A Facile Single-Step Synthesis of Nitrogen-Doped Reduced Graphene Oxide-Mn_3O_4 Hybrid Functional Material for the Electrocatalytic Reduction of Oxygen.

ARTICLE *in* ACS APPLIED MATERIALS & INTERFACES · JANUARY 2014

Impact Factor: 6.72 · DOI: 10.1021/am405213z · Source: PubMed

4 AUTHORS, INCLUDING:

Sourav Bag
IIT Kharagpur
11 PUBLICATIONS **228** CITATIONS
SEE PROFILE

Kanak Roy
CSIR - National Chemical Laboratory, Pune
9 PUBLICATIONS **107** CITATIONS
SEE PROFILE

C Retna Raj
IIT Kharagpur
91 PUBLICATIONS **3,197** CITATIONS
SEE PROFILE

ACS APPLIED MATERIALS & INTERFACES

Research Article

www.acsami.org

Facile Single-Step Synthesis of Nitrogen-Doped Reduced Graphene Oxide-Mn_3O_4 Hybrid Functional Material for the Electrocatalytic Reduction of Oxygen

Sourav Bag,[†] Kanak Roy,[‡] Chinnakonda S. Gopinath,[‡,§] and C. Retna Raj*[,†]

[†]Functional Materials and Electrochemistry Laboratory, Department of Chemistry, Indian Institute of Technology, Kharagpur 721302, West Bengal, India

[‡]Catalysis Division and [§]Center of Excellence on Surface Science, CSIR-National Chemical Laboratory, CSIR-National Chemical Laboratory, Dr. Homi Bhabha Road, Pune 411 008, India

Supporting Information

ABSTRACT: Development of efficient electrocatalyst based on non-precious metal that favors the four-electron pathway for the reduction of oxygen in alkaline fuel cell is a challenging task. Herein, we demonstrate a new facile route for the synthesis of hybrid functional electrocatalyst based on nitrogen-doped reduced graphene oxide (N-rGO) and Mn_3O_4 with pronounced electrocatalytic activity towards oxygen reduction reaction (ORR) in alkaline solution. The synthesis involves one-step in situ reduction of both graphene oxide (GO) and Mn(VII), growth of Mn_3O_4 nanocrystals and nitrogen doping onto the carbon framework using a single reducing agent, hydrazine. The X-ray photoelectron (XPS), Raman and FTIR spectral, and X-ray diffraction measurements confirm the reduction of GO and growth of nanosized Mn_3O_4. The XPS profile reveals that N-rGO has pyridinic (40%), pyrrolic (53%), and pyridine N oxide (7%) types of nitrogen. The Mn_3O_4 nanoparticles are single crystalline and randomly distributed over the wrinkled N-rGO sheets. The hybrid material has excellent ORR activity and it favors the 4-electron pathway for the reduction of oxygen. The electrocatalytic performance of the hybrid catalyst is superior to the N-rGO, free Mn_3O_4 and their physical mixture. The hybrid material shows an onset potential of −0.075 V, which is 60−225 mV less negative than that of the other catalyst tested. It has excellent methanol tolerance and high durability. The catalytic current density achieved with the hybrid material at 0.1 mg cm^{-2} is almost equivalent to that of the commercial Pt/C (10%). The synergistic effect of N-rGO and Mn_3O_4 enhances the overall performance of the hybrid catalyst. The nitrogen in N-rGO is considered to be at the interface to bridge the rGO framework and Mn_3O_4 nanoparticles and facilitates the electron transfer.

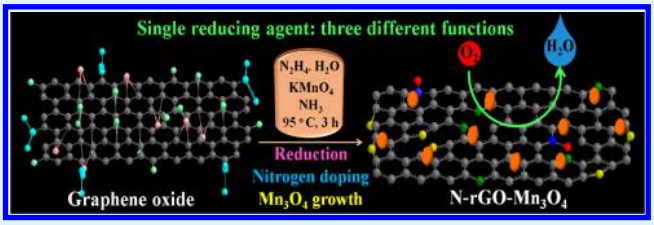

KEYWORDS: *hybrid material, nitrogen-doped graphene, Mn_3O_4, oxygen reduction, electrocatalysis, synergistic effect*

INTRODUCTION

Synthesis of the metal-free or nonprecious metal-based electrocatalysts for oxygen reduction reaction (ORR) is of great importance in the development of energy conversion devices like fuel cells and metal−air batteries.[1] Development of such energy conversion devices is in demand owing to the global energy crisis. Traditionally, platinum (Pt) and Pt-based alloy catalyst have been used as a catalyst in the cathode compartment of these devices.[2,3] The major barriers in the successful commercialization of fuel cells are (i) high cost of Pt because of its scarcity and (ii) sluggish electron transfer kinetics associated with the cathode reaction. It has been estimated that 30−50% of the manufacturing cost of the fuel cell is actually due to both anode and cathode catalysts.[3] The high cost and lack of durability of the Pt-based catalysts demand for an alternative cost-effective highly efficient catalyst.[4] The nitrogen-based electrocatalysts have been examined since 1964, as an alternative catalyst for ORR.[5] For instance, Yeager's group, for the first time, demonstrated the electrocatalytic ORR activity of nitrogen-based catalyst derived by the pyrolysis of acrylonitrile polymer and metal salts.[6] The transition metal−nitrogen center was considered to be the active site for the catalytic reduction of oxygen to hydrogen peroxide. Although such catalysts are known to be active towards ORR, the actual electrocatalytic properties of nitrogen-based catalysts are being explored only recently. The carbon-supported nonprecious metal−N_4 macrocyclic complexes and the catalyst derived by the pyrolysis of carbon−nitrogen template and non-precious metal salts have been proposed as an electrocatalyst for ORR.[7,8] Inspired by the better electrocatalytic performance of these nitrogen-based catalyst, various groups have shown interest in the synthesis of nitrogen containing various forms of carbon (nanofiber, nanotubes, etc.) and investigated the electrocatalytic activity.[9,10] Very recently, graphene, the one atom thick honeycomb carbon lattice, and the heteroatom-doped graphene are exploited for various electrocatalytic applications.[11,12] The unique physical

Received: November 19, 2013
Accepted: January 29, 2014
Published: January 29, 2014

   dx.doi.org/10.1021/am405213z | ACS Appl. Mater. Interfaces 2014, 6, 2692−2699

and chemical features of this one-atom-thick carbon framework are very promising for the development of energy conversion devices.[13] Recently, the ORR activity of the nitrogen-doped graphene-based catalysts has been explored. It has been found that the metal-free nitrogen-doped graphene has good electrocatalytic activity with respect to the traditional carbon-supported Pt catalyst. The electrocatalytic activity of nitrogen-doped graphene depends on various factors such as nature and amount of nitrogen, defects in the carbon framework, etc. Ruoff's group demonstrated that the graphitic and pyridinic nitrogen of the carbon framework have major contribution in the enhanced electrocatalytic performance of nitrogen-doped graphene towards ORR.[14]

The functional materials based on the transition metal oxides have also been exploited for various electrocatalytic applications. The oxides of cobalt, iron, iridium, manganese, etc., have been pursued as an alternative nonprecious metal catalyst for ORR.[15−18] The theoretical and experimental studies have demonstrated that the transition metal oxides with spinel structure are very promising electrode material for energy conversion and storage applications.[19−22] The mixed valence manganese oxides like Mn_3O_4 have received special attention because of the fact that they are highly active, inexpensive, and environment friendly.[23] Although these oxide materials have been well-exploited for battery and supercapacitor applications, only a handful papers describes their electrocatalytic activity towards ORR.[24−27] For instance, Ohsaka's group demonstrated the catalytic two-step reduction of oxygen in alkaline medium using unsupported manganese oxides, including the mixed valence Mn_3O_4.[24,25] Very recently, Jaramillo's group has shown the electrocatalytic performance of heat-treated porous Mn_3O_4 supported on glassy carbon electrode towards ORR.[26] Carbon-supported Mn_2O_3 have also been explored as ORR catalyst.[25−27] The low electrical conductivity of manganese oxides is a major concern in utilizing them as an active catalyst for ORR.[28,29] The low electrical conductivity can be circumvented by developing a hybrid material of Mn_3O_4 and conducting functional support materials.

The functional hybrid materials derived from the inorganic metal oxides and honeycomb carbon have received special attention in recent years for different electrochemical applications. One of the major advantages of developing such hybrid material is that the unique properties of individual component can be integrated together without compromise. The integration of Mn_3O_4 with graphene would circumvent the problem associated with its low conductivity, as graphene is known to have very high electronic conductivity. Recently, Kim's group demonstrated the use of such hybrid material for Zn-air battery application.[30] Dai's group reported the ORR activity of electrically interconnected hybrid material based on graphene oxide-carbon nanotubes-Mn_3O_4 synthesized by a two-step method.[31] During the course of our investigation Qiao's group demonstrated the synthesis of mesoporous Mn_3O_4-nitrogen doped graphene by a solvothermal route and its electrocatalytic activity. The reduction of graphene oxide (GO), nitrogen doping and growth of Mn_3O_4 nanoparticles were achieved in two steps; the synthetic method involves the use of Teflon-lined stainless steel autoclave at elevated temperature for 13 h.[32] Doping of nitrogen has been achieved by various methods involving multiple steps, tedious procedures, high temperature, and sophisticated equipments.[33,34] Although hydrazine has been used as a nitrogen doping agent in the recent past, the procedures are either tedious or time consuming.[35−38] Development of a rapid and simple protocol for the synthesis of hybrid material of nitrogen-doped graphene and Mn_3O_4 is highly desired for catalytic applications. Herein we demonstrate a single-step facile route for the rapid synthesis of functional nitrogen-doped reduced graphene oxide-Mn_3O_4 (N-rGO-Mn_3O_4) hybrid material with pronounced electrocatalytic activity towards oxygen reduction. Interestingly, our synthetic method involves one-pot procedure using a single reducing agent without hydrothermal/solvothermal conditions. The novelty of our method is the use of hydrazine as a multifunctional reagent for the reduction of GO and Mn(VII), doping of nitrogen, and the growth of Mn_3O_4 nanoparticles in single-step. To the best of our knowledge, this is the first report describing the multiple function of hydrazine in the synthesis of hybrid catalytic materials. Our hybrid material is highly active with an onset potential of −0.075 V (SCE), which is significantly more positive than the existing Mn_3O_4-based electrode, and it is highly durable with a high tolerance toward methanol.

MATERIALS AND METHODS

Reagents and Materials. Graphite powder, poly(vinylidene fluoride) (PVF), and Pt/C (10%) were purchased from Sigma-Aldrich. Analytical grade $KMnO_4$, $NaNO_3$, H_2SO_4 and NH_3, HCl, hydrazine hydrate were obtained from Merck, India. All the solutions were made of Millipore water (Milli Q system).

Exfoliation of Graphite and Synthesis of GO. Graphene oxide was synthesized according to modified Hummer's method by the exfoliation of graphite.[39,40] Briefly, 50 mL of concentrated H_2SO_4 was slowly added to a mixture of graphite powder (1 g) and $NaNO_3$ (1 g) in a 500 mL round-bottom flask at 0 °C. Then solid $KMnO_4$ (6 g) was added to the reaction mixture and the reaction mixture was stirred continuously for 1 h at room temperature. The mixture was then diluted with 200 mL of water and after 15 min, H_2O_2 solution (30%) was added to the reaction mixture under stirring until the gas evolution was ceased. The residue was then separated from the reaction mixture by centrifugation and then washed repeatedly with 5% HCl solution. The washing was continued until the centrifugate gave a negative test for the presence of sulphate ions with $BaCl_2$ solution. The residue obtained after repeated washing was further washed with copious amounts of Millipore water and dried in a vacuum to get the yellow-brown solid of GO.

Synthesis of Free Mn_3O_4 and N-rGO-Mn_3O_4 Hybrid Material. In a typical synthesis, 20 mg of GO was dispersed in 40 mL of water and sonicated in an ultrasonicator for an hour. Then, 10 mL of aqueous $KMnO_4$ solution (1 mg/mL) was mixed with the GO dispersion and the mixture was transferred to a round bottomed flask. Then 200 μL of NH_3 (25%) solution was added to the mixture under constant stirring. Hydrazine hydrate (200 μL, 99%) was then slowly added to the reaction mixture and refluxed for 3 h at 95 °C. The final concentration of hydrazine in the reaction mixture was 4 mM. The black colored solution was centrifuged and the product was washed well with copious amount of water and alcohol and dried in vacuum. The free Mn_3O_4 was synthesized at an identical procedure without GO. During the synthesis of free Mn_3O_4, the purple color of $KMnO_4$ initially turned to brown and then finally to orange-brown. Hereafter, the hybrid material is designated as N-rGO-Mn_3O_4 whereas the physical mixture of Mn_3O_4 with N-rGO and rGO are designated as N-rGO/Mn_3O_4 and rGO/Mn_3O_4.

Electrode Modification. The glassy carbon (GC) rotating disk electrode (RDE) and GC-Pt rotating ring-disk electrode (RRDE) were polished well with fine emery paper and alumina (0.05 μm) slurry and sonicated in Millipore water for 10-15 min to remove the physically adsorbed impurities. These electrodes were washed repeatedly with copious amount of Millipore water and dried in argon atmosphere. The catalyst ink was prepared by mixing 0.4 mg of N-rGO-Mn_3O_4 with 200 μL N-methyl-2-pyrrolidone containing PVF (1 mg/mL) and

Scheme 1. Scheme Illustrating the One-Pot Synthesis of N-rGO-Mn_3O_4 Hybrid Material

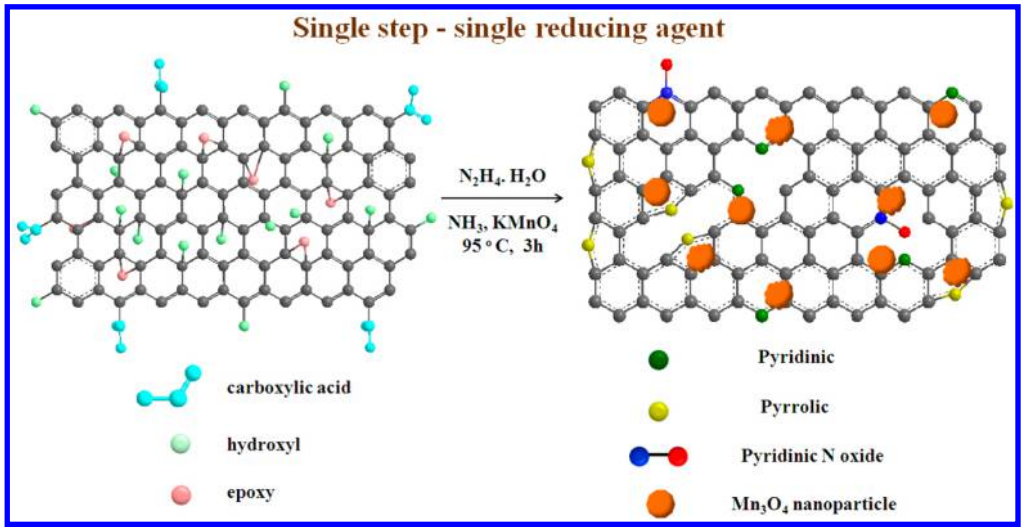

sonicating for 2 h. An aliquot of 10 μL of the ink was drop casted on the surface and dried in ambient temperature. The mass loading of the catalysts on the electrode surface was kept at 0.1 mg/cm^2.

Material Characterization. Transmission electron microscopic (TEM) measurements were performed with JEOL JEM 2010 at an operating voltage of 200 kV. Field-emission scanning electron microscopic (FESEM) analysis was carried out with Carl Zeiss Supra 40. Energy dispersive X-ray microanalyzer (OXFORD ISI 300 EDAX) attached to the electron microscope was used for elemental compositional analysis of the hybrid material. X-ray diffraction (XRD) analysis was carried out with a BRUKER D8 Advance XRD unit using Cu−K_α (λ = 1.54 Å) radiation. Perkin Elmer Spectrum 1 RX 1 FTIR spectrometer was used for the FTIR analysis. XPS analysis was performed at 1 × 10^{-10} mbar pressure with custom-built laboratory version ambient pressure photoelectron spectrometer (Lab-APPES).[41] Electrochemical experiments were performed in a two-compartment three electrode cell with saturated calomel (SCE) as reference, a Pt wire as counter and GC RDE or GC-Pt RRDE as working electrodes. The polarization curves were recorded with an Autolab potentiostat/galvanostat (302N) workstation with a computer controlled GPES software and PINE electrode rotating instruments (USA). All the experiments have been performed at least three times and reproducible results were obtained.

RESULTS AND DISCUSSION

Synthesis and Characterization of N-rGO-Mn_3O_4. Scheme 1 illustrates the single-step synthesis of N-rGO-Mn_3O_4 hybrid material. The synthetic protocol involves the in situ reduction of both GO and Mn(VII), nitrogen doping onto the carbon framework and growth of Mn_3O_4 over N-rGO in one pot. Hydrazine hydrate actually plays two important roles in the synthesis as a reducing as well as doping agent. Simultaneous reduction of both GO and Mn(VII) ions has been achieved with a single reducing agent. During the reduction of GO, nitrogen is being doped into the graphene framework. The concentration of hydrazine is very critical to achieve the reduction of GO and Mn(VII) ions and nitrogen doping. An optimized amount of 4 mM of hydrazine is required for the reduction of both GO and Mn(VII) and doping of the carbon framework. Although low concentration of hydrazine (< 4 mM) is sufficient enough for the reduction, effective doping of nitrogen was not achieved. The percentage of nitrogen on the carbon framework was less (N/C ratio ≤0.05) at low concentration of hydrazine. Figure 1A is the XRD profile obtained for free Mn_3O_4 and N-rGO-Mn_3O_4 hybrid material.

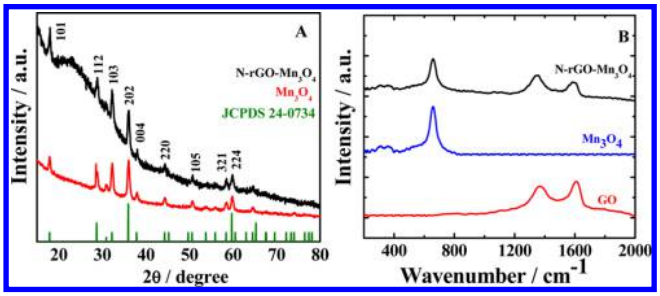

Figure 1. (A) XRD profile and (B) Raman spectra of Mn_3O_4 nanoparticles, N-rGO-Mn_3O_4 hybrid material and GO.

The diffraction profile shows characteristic signature (JCPDS 24-0734) for tetragonal hausmannite crystal structure of Mn_3O_4. All the peaks were indexed according to the JCPDS file No. 24-0734. No additional peaks were observed, confirming the absence of other manganese oxides or impurity. The lattice constants were calculated from the diffraction profile and were $a = b = 5.78$ and $c = 9.467$ Å, which are in agreement with the anticipated value for Mn_3O_4 from JCPDS file.[42] The broad peak in the range between 22 and 24° is assigned to the disordered rGO layers.[43] The exfoliation and chemical oxidation essentially increases interlayer spacing with respect to graphite. The characteristic signature at 10.4° for GO is completely absent. The Raman spectral profile for GO, free Mn_3O_4, and N-rGO-Mn_3O_4 is shown in Figure 1B. The Raman spectra of GO show characteristic D and G bands at 1364 and 1604 cm^{-1}, respectively. The D and G band ratio (I_D/I_G) for GO is 0.811. The D band is associated with the structural defects, whereas the G band corresponds to the E_{2g} mode for sp^2 carbon domain. In the case of N-rGO-Mn_3O_4, a 14−22 cm^{-1} red shift of both D and G bands was observed. It is generally accepted that the relative intensity ratio of these bands is a measure of the disorder and extent of defects in the graphitic materials. A significant increase in the ratio (I_D/I_G =1.31) of these bands was observed for the N-rGO-Mn_3O_4, indicating the increase in the (i) defects due to nitrogen doping onto the conjugated carbon framework and (ii) disorder of rGO layers.[44,45] The G band of N-rGO-Mn_3O_4 shifted to 1590 cm^{-1} and it can be attributed to doping or strain effect.[46,47] The sharp and predominant peak at 660 cm^{-1} and the small peaks ~310 and 370 cm^{-1} for both free Mn_3O_4 and N-rGO-Mn_3O_4

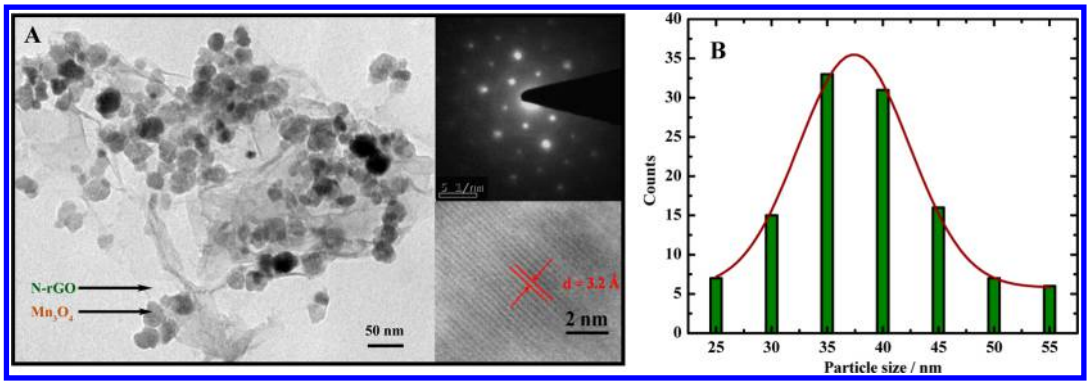

Figure 2. (A) TEM image and (B) the corresponding histogram of the hybrid material. HRTEM image and SAED pattern are shown in inset.

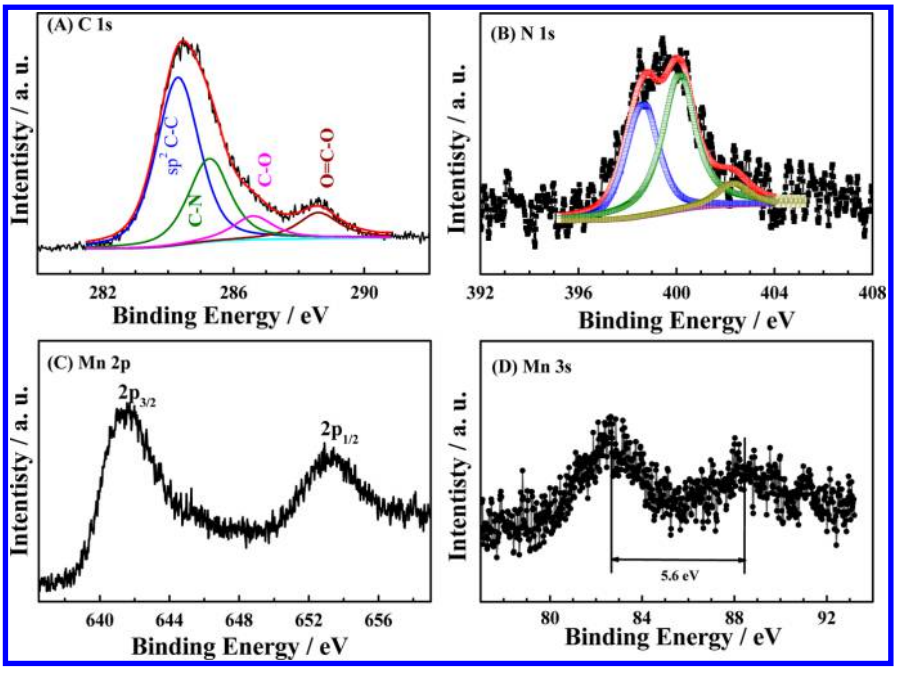

Figure 3. Deconvoluted XPS profile of N-rGO-Mn_3O_4 hybrid material: (A) C 1s, (B) N 1s, (C) Mn 2p, and (D) Mn 3s. The survey scan spectrum is given in the Supporting Information.

are associated with the crystalline Mn_3O_4 nanoparticles.[20,48] It is interesting to note that the hybrid material retains the structural integrity of both rGO and Mn_3O_4. The FTIR spectral measurements further confirm the reduction of oxygen containing functional groups of GO. Significant decrease in the intensity of the peaks corresponding to the oxygen containing functionalities has been noticed. Moreover, characteristic signature for the coupling corresponding to the Mn−O stretching modes of tetrahedral and octahedral manganese is also observed (see the Supporting Information).

The shape and structural morphology of N-rGO-Mn_3O_4 were analyzed by TEM measurements (Figure 2). The presence of wrinkled rGO sheets and random distribution of Mn_3O_4 naonparticles over the sheet are clearly seen in the image. The nanoparticles have quasi spherical shape with an average size of 40 nm. The histogram shows that >30% of the particles have the size of 37 nm. The selected area electron diffraction (SAED) pattern was obtained by focusing the electron beam on the Mn_3O_4 naoparticles and it shows well-defined spotty pattern confirming that the nanoparticles are actually single crystalline. The high-resolution image shows the fringe spacing of 0.32 nm, corresponding to the (112) plane of spinel Mn_3O_4. The SAED pattern and HRTEM image are consistent with the XRD profile shown in Figure 1A. EDS measurement performed with the hybrid material confirms the presence of C, Mn, N and O. The atomic percentage of C, N, O and Mn was found to be 72.36, 5.35, 14.12, and 8.03, respectively (see the Supporting Information). The nitrogen-to-carbon elemental ratio (N/C) was calculated to be 0.073. The FESEM and elemental mapping analysis further confirm the presence of these elements in the hybrid material (see the Supporting Information).

To understand the composition and chemical nature of N-rGO-Mn_3O_4 hybrid material, XPS measurements have been performed. The survey scan spectrum shows the signature for C, N, O, and Mn (see the Supporting Information). C1s spectrum of GO show a broad peak at 284.5 with shoulder at high binding energy and another small peak at 288.6 eV. To resolve the contribution of different types of carbon, deconvolution was employed. The deconvoluted C1s spectrum of GO has two main peaks centred at 284.34 and 286.4 eV and a small peak at 288.6 eV in agreement with the literature. The peak at 284.34 eV is attributed to the binding energy of sp^2 C−C bond and the peak at 286.4 eV is associated with C−O bonds in epoxy/hydroxyl/carbonyl group of GO. The small peak is

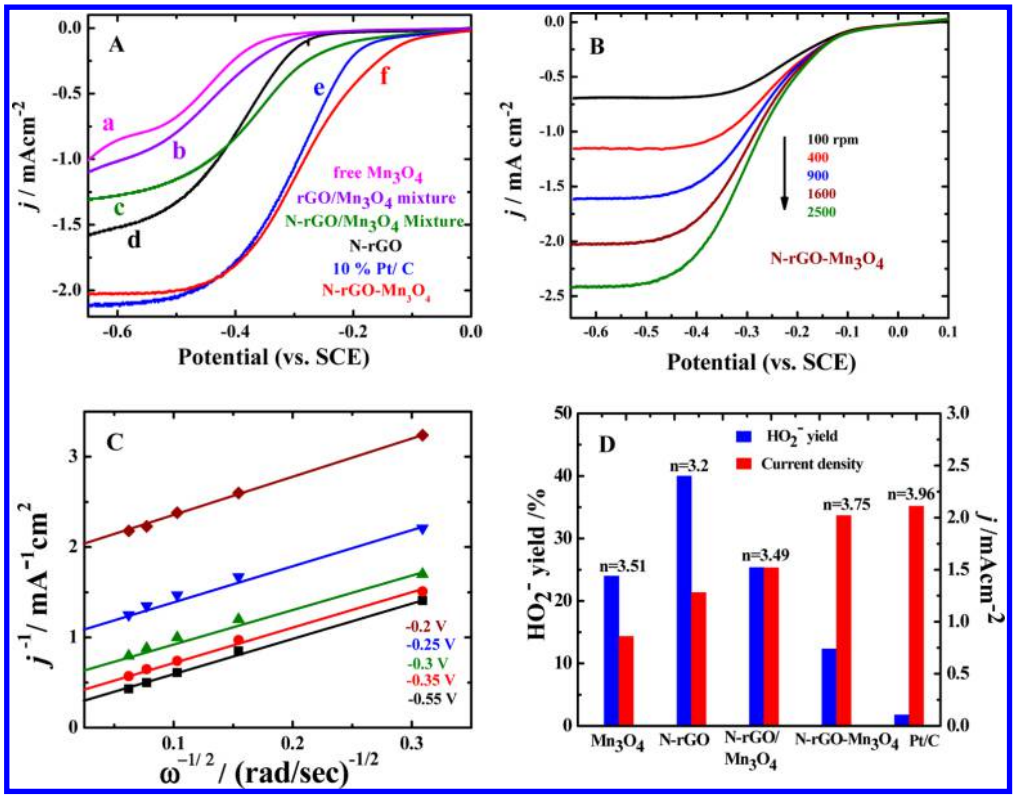

Figure 4. (A) Polarization curves illustrating the electrocatalytic performance of (a) free Mn_3O_4, (b) rGO/Mn_3O_4 mixture, (c) N-rGO, (d) N-rGO/Mn_3O_4 mixture, (e) 10% Pt/C, and (f) hybrid N-rGO-Mn_3O_4 towards ORR at 1600 rpm. (B) Polarization curves at different rotation with the hybrid catalyst and the (C) corresponding K-L plot for the hybrid material at different potentials. (D) Plot illustrating the percentage of peroxide yield, current density and number of electrons transferred with all the catalyst. Peroxide yield, current density and number of electrons were calculated using the ring/disk current at the potential of −0.6 V. Supporting electrolyte: O_2 saturated 0.1 M KOH. Scan rate: 5 mV/s.

attributed to the C═O and O−C═O functionalities of GO.[38,49,50] In the C1s spectrum of N-rGO-Mn_3O_4, the peak corresponding to C−C became predominant and the intensity of the characteristic peaks for the oxygen containing functionalities significantly decreased, though not completely vanished (Figure 3A). The decrease in the intensity of the peaks at 286.4 and 288.6 eV is in good agreement with FTIR results (see the Supporting Information), confirming the successful removal of most of the oxygen containing hydroxyl and epoxide functionalities. Carbon associated with nitrogen appears at 285.3 eV, which is distinctly seen on deconvolution, suggesting the introduction of nitrogen into the rGO sheets. The nitrogen doping onto the carbon framework was further confirmed by XPS analysis. The deconvoluted N 1s spectra (Figure 3B) shows signature for pyridinic (40%), pyrrolic (53%), and pyridinic N oxide nitrogen (7%) at 398.66, 400.12, and 402.32 eV, respectively.[9,11] The close examination of XPS profile shows that the hybrid material has N/C elemental ratio of 0.07 and 40% of the total nitrogen is of pyridinic in nature. The N/C elemental ratio from XPS measurement is in excellent agreement with the EDS measurement (vide supra).The presence of large amount of pyridinic nitrogen is advantageous, as the graphene doped with pyridinic nitrogen is known to be electrocatalytically highly active towards ORR.[9,14] Mn 2p and 3s core levels were analyzed in N-rGO-Mn_3O_4 hybrid material to know the changes in oxidation state of Mn and the results are given in Figure 3C and D, respectively. The peaks observed at 641.5 and 653.2 eV correspond to Mn $2p_{3/2}$ and Mn $2p_{1/2}$, respectively. This binding energy corresponds to the oxidation state of Mn(II) and Mn(III) and it is difficult to distinguish. The energy separation between these peaks is 11.7 eV, which is in agreement with the earlier literature on mixed valent Mn_3O_4.[51,52] In the Mn 3s spectra, two peaks at 82.8 and 88.4 eV with the separation of 5.6 eV were observed (Figure 3D); the exchange interaction between the electrons in 3s and other unpaired electrons cause the splitting of 3s spectra and is in accordance with the previous literature.[20] The Mn 3s splitting value of 5.6 eV is corresponding to the mixed valence state of Mn(II) and Mn(III).[51,52]

Electrocatalytic Reduction of Oxygen. The ORR activity of N-rGO-Mn_3O_4 hybrid material was explored using hydrodynamic voltammetry. The catalytic performance of the hybrid materials was compared with free Mn_3O_4 nanoparticles, N-rGO, 10% Pt/C and the physical mixture of Mn_3O_4 with N-rGO and rGO (N-rGO/Mn_3O_4 and rGO/Mn_3O_4). Figure 4A is the polarization curves registered for these catalysts in 0.1 M KOH solution at 1600 rpm. As can be seen, the N-rGO-Mn_3O_4 hybrid material shows the onset potential for the reduction of oxygen at -0.075 V, which is 60-225 mV less negative than that of rGO/Mn_3O_4, Pt/C, free Mn_3O_4 ,and N-rGO/Mn_3O_4. The well-defined polarization curve obtained on the N-rGO-Mn_3O_4 hybrid material-based electrode indicates the facilitated electron transfer kinetics for ORR. The current density at the potential of -0.6 V on N-rGO-Mn_3O_4 is 1.3-2.3 times higher than that of the N-rGO and free Mn_3O_4 and is very close to that of Pt/C. It should be noted here that catalytic current density achieved with the hybrid material at the mass loading of 0.1 mg cm^{-2} is equivalent to that of 10% Pt/C at the same loading. The kinetics of ORR was further examined by registering the hydrodynamic voltammograms at different rotations of the

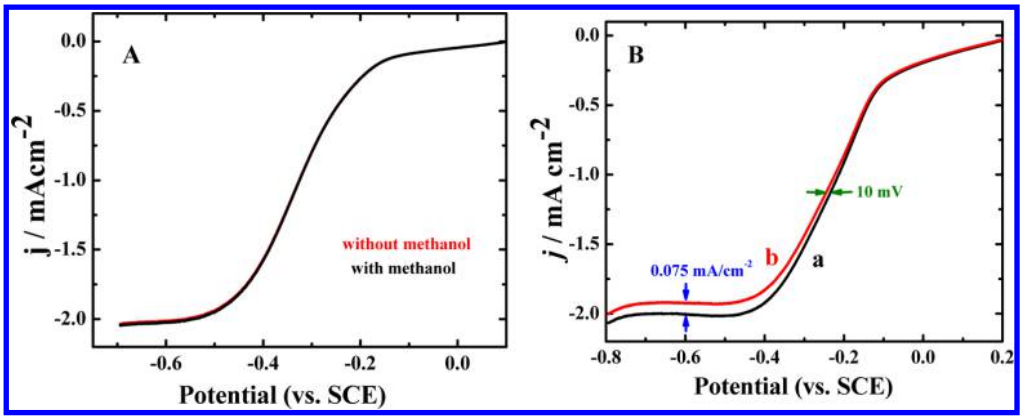

Figure 5. Polarization curves illustrating (A) methanol tolerance and (B) durability of the hybrid material. Methanol tolerance was examined in the oxygen saturated solution containing methanol (1 M). The durability test was performed using the same electrode for 3000 extensive cycles. The overlaid curves were obtained (a) before and (b) after 3000 extensive potential cycles.

electrode and analyzing with Koutecky–Levich (K–L) plot (Figure 4C and the Supporting Information). The linear increase in the limiting current implies a diffusion limited electron transfer reaction on the catalyst-modified electrodes. The K–L plot has similar slopes at different potential, suggesting that the number of electrons (n) transferred is almost same at all the potentials (vide infra). It is worth pointing out here that the catalytic activity of the N-rGO-Mn_3O_4 hybrid material is superior to that of the physical mixture of free N-rGO and Mn_3O_4, indicating the existence of strong integration between N-rGO and Mn_3O_4 and synergistic effect of the hybrid. The synergistic effect of N-rGO and Mn_3O_4 actually facilitate the electron transfer for ORR. Polarization curves were registered with RRDE to understand the reaction pathway. The n value for ORR and the percentage of HO_2^- generated during the reaction was obtained according to the literature procedures[16] (Figure 4D and the Supporting Information). The n value and the percentage of HO_2^- depend on the electrode potential (Supporting Information). For the N-rGO-Mn_3O_4 hybrid material, the average value of n was 3.8, which is close to 4 for the direct reduction of oxygen to water. The percentage of HO_2^- during ORR varies between 5 and 12.3% in the potential range of −0.2 to −0.6 V on the N-rGO-Mn_3O_4 hybrid material, suggesting that the catalyst mainly favors the four-electron pathway for ORR. However, in the cases of free Mn_3O_4, N-rGO, and the physical mixture, the HO_2^- yield was >25% (Figure 4D), indicating that ORR involves a mixed electron transfer pathway. It should be noted here that both free Mn_3O_4 and the physical mixture have similar HO_2^- yield and n value, implying that the property of the physical mixture is similar to that of free Mn_3O_4 and is largely different from the hybrid material.

The pronounced catalytic activity of N-rGO-Mn_3O_4 can be explained by considering the synergistic effect. Recently, Ruoff's group demonstrated the effect of nitrogen doping in ORR and concluded that the catalytic activity of nitrogen-doped graphene depends on the nature and amount of nitrogen content.[14] It has been shown that the graphitic nitrogen actually enhances the limiting current whereas the pyridinic nitrogen shifts the onset potential for ORR. The pyridinic nitrogen favors the direct reduction pathway for ORR. The careful examination of the XPS profile reveals that N-rGO-Mn_3O_4 has 40% of pyridinic nitrogen. One can account the enhanced activity to the existence of pyridinic nitrogen. However, the catalytic performance of free N-rGO in terms of onset potential and current density is poor; the onset potential is 165 mV more negative and the current density is 26% less than that of the hybrid material. The poor activity could be due to the coexisting pyrrolic nitrogen on the carbon framework. Moreover, N-rGO favors the mixed electron transfer pathway for ORR and the yield of HO_2^- >40%, which is significantly higher than the hybrid material. (Figure 4D). It is concluded that the pronounced electrocatalytic activity is essentially originates from the synergistic effect of both Mn_3O_4 and N-rGO; the synergistic effect is mostly due to nitrogen being at the interface in the hybrid material. The integration of Mn_3O_4 with N-rGO enables in overcoming the slow electron conduction in Mn_3O_4 and very likely, the interface between the above constituents plays a major role in increasing the overall catalytic performance. Probably, nitrogen from N-rGO may be at the interface to bridge the constituents and facilitate the electron transfer. It is worth pointing out here that the electrocatalytic performance of the physical mixture of undoped rGO and Mn_3O_4 is inferior to the other catalyst tested (Figure 4). It strongly supports that the nitrogen of the N-rGO-Mn_3O_4 hybrid actually plays a key role in facilitating the electron transfer for ORR.

The durability and methanol tolerance are the two major concerns with the traditional Pt-based electrocatalyst. Although Pt-based catalysts are known to be catalytically active, they have methanol intolerance and are not durable. The N-rGO-Mn_3O_4 hybrid material has excellent tolerance towards methanol; polarization curves were recorded for ORR in the presence of high concentration of methanol (1 M) and the voltammetric response is essentially the same as in the absence of methanol, confirming that the new hybrid material has excellent tolerance towards methanol (Figure 5A). The hybrid material does not catalyze the oxidation of methanol in the potential window used for ORR. It is interesting to note that the presence of methanol does not alter the electrocatalytic performance of the hybrid material towards ORR. The methanol tolerance was further examined by registering the amperometric i–t curve in the absence and presence of methanol (1 M). The amperometric current on N-rGO-Mn_3O_4 does not change even after the addition of high concentration of methanol, ascertaining the high tolerance of the hybrid material. It is worth to point out here that a large increase in the current was noticed for Pt/C upon the addition of methanol, indicating the intolerance of Pt/C towards methanol. It is known that the Pt-based catalysts are capable of catalyzing the oxidation of methanol. The durability of the hybrid material was examined

by registering the polarization and amperometric $i-t$ curve in O_2-saturated 0.1 M KOH electrolyte. The electrode was subjected to extensive potential cycling in between 0.2 and −0.8 V. The polarization curve obtained before and after 3000 cycles shows only a 4% decrease in the limiting current. Interestingly, no significant change in the onset potential was noticed; only 10 mV negative shift in the half-wave potential was noticed after extensive 3000 cycles, implying the high durability of the hybrid catalyst (Figure 5B). The amperometric measurement further confirms the durability of the hybrid material. Only a 14% decrease in the initial current was observed after 10000 s of the measurement. In the case of Pt/C, more than 42% decrease in the initial current was obtained during the durability test (see the Supporting Information).

SUMMARY

In summary, a facile chemical route for the single-step synthesis of hybrid material based on N-rGO and Mn_3O_4 and the electrocatalytic performance toward ORR have been demonstrated. The novelty of our synthetic method is that nitrogen doping of carbon framework and reduction of both GO and Mn(VII) have been achieved in single step using a single reducing agent for the first time. The Mn_3O_4 nanoparticles on the N-rGO sheets have an average size of 37 nm. The spotty SAED pattern suggests the single crystalline nature of the Mn_3O_4 nanoparticles. The hybrid material has excellent electrocatalytic activity towards ORR in alkaline solution and it favors the four electron reduction of oxygen to water. Unlike N-rGO and free Mn_3O_4 nanoparticles, the hybrid material show high current density and less negative onset potential. The overall catalytic performance is superior to that of the N-rGO, free Mn_3O_4, and their physical mixture. It is highly durable and has excellent tolerance towards methanol. The performance of our hybrid catalyst in terms of current density, onset potential, durability, and methanol tolerance implies the synergistic effect of the hybrid. The major advantage of the in situ synthetic protocol is the integration of the individual properties of both N-rGO and Mn_3O_4 in single-step without compromising the catalytic activity. The integration of the individual property actually enhances the overall performance of the hybrid catalyst. The current density achieved with the hybrid material at 0.1 mg cm^{-2} loading is nearly equivalent to that of 10% Pt/C at the same loading. Our study suggests that N-rGO-Mn_3O_4 hybrid material can be effectively used as cathode catalyst in alkaline fuel cell.

ASSOCIATED CONTENT

Supporting Information

XRD, FTIR, and XPS profile of GO and N-rGO-Mn_3O_4; RRDE response, plot illustrating the percentage of HO_2^- generated and electron transfer number at different potential, amperometric i-t plots, EDS and FESEM, and mapping images. This material is available free of charge via the Internet at http://pubs.acs.org/.

AUTHOR INFORMATION

Corresponding Author

*E-mail: crraj@chem.iitkgp.ernet.in.

Notes

The authors declare no competing financial interest.

ACKNOWLEDGMENTS

This work was financially supported by Department of Science and Technology, New Delhi. SB is a recipient of UGC research fellowship. We gratefully acknowledge DST-FIST for the XRD facility.

REFERENCES

(1) Bashyam, R.; Zelenay, P. *Nature* **2006**, *443*, 63−66.
(2) Ghosh, S.; Sahu, R. K.; Raj, C. R. *Nanotechnology* **2012**, *23*, 385602−385609.
(3) Ghosh, S.; Sahu, R. K.; Raj, C. R. *Catal. Sci. Technol.* **2013**, *3*, 1078−1085.
(4) Morozan, A.; Jousselme, B.; Palacin, S. *Energy Environ. Sci.* **2011**, *4*, 1238−1254.
(5) Jasinski, R. *Nature* **1964**, *201*, 1212−1213.
(6) Gupta, S.; Tryk, D.; Bae, I.; Aldred, W.; Yeager, E. *J. Appl. Electrochem.* **1989**, *19*, 19−27.
(7) Liu, R.; Malotki, C.; Arnold, L.; Koshino, N.; Higashimura, H.; Baumgarten, M.; Müllen, K. *J. Am. Chem. Soc.* **2011**, *133*, 10372−10375.
(8) Wu, G.; More, K. L.; Johnston, C. M.; Zelenay, P. *Science* **2011**, *332*, 443−447.
(9) Rao, C. V.; Cabrera, C. R.; Ishikawa, Y. *J. Phys. Chem. Lett.* **2010**, *1*, 2622−2627.
(10) Maldonado, S.; Stevenson, K. J. *J. Phys. Chem. B* **2005**, *109*, 4707−4716.
(11) Yang, S.; Zhi, L.; Tang, K.; Feng, X.; Maier, J.; Müllen, K. *Adv. Funct. Mater.* **2012**, *22*, 3634−3640.
(12) Pan, F.; Jin, J.; Fu, X.; Liu, Q.; Zhang, J. *ACS Appl. Mater. Interfaces* **2013**, *5*, 11108−11114.
(13) Kamat, P. V. *J. Phys. Chem. Lett.* **2011**, *2*, 242−251.
(14) Lai, L.; Potts, J. R; Zhan, D.; Wang, L.; Poh, C. K.; Tang, C.; Gong, H.; Shen, Z.; Lin, J.; Ruoff, R. S. *Energy Environ. Sci.* **2012**, *5*, 7936−7942.
(15) Zhou, W.; Ge, L.; Chen, Z. G.; Liang, F.; Xu, H. Y.; Motuzas, J.; Julbe, A.; Zhu, Z. *Chem. Mater.* **2011**, *23*, 4193−4198.
(16) Wu, Z. S.; Yang, S.; Sun, Y.; Parvez, K.; Feng, X.; Müllen, K. *J. Am. Chem. Soc.* **2012**, *134*, 9082−9085.
(17) Liang, Y. Y.; Li, Y. G.; Wang, H. L.; Zhou, J. G.; Wang, J.; Regier, T.; Dai, H. *Nat. Mater.* **2011**, *10*, 780−786.
(18) Chang, C. H.; Yuen, T. S.; Nagao, Y.; Yugami, H. *J. Power Sources* **2010**, *195*, 5938−5941.
(19) Behera, S. K. *Chem. Commun.* **2011**, *47*, 10371−10373.
(20) Lee, J. W.; Hall, A. S.; Kim, J. D.; Mallouk, T. E. *Chem. Mater.* **2012**, *24*, 1158−1164.
(21) Liang, Y.; Wang, H.; Zhou, J.; Li, Y.; Wang, J.; Regier, T.; Dai, H. *J. Am. Chem. Soc.* **2012**, *134*, 3517−3523.
(22) Arico, A. S.; Bruce, P.; Scrosati, B.; Tarascon, J. M.; Schalkwijk, W. V. *Nat. Mater.* **2005**, *4*, 366−377.
(23) Wang, Y.; Cheng, L.; Li, F.; Xiong, H.; Xia, Y. *Chem. Mater.* **2007**, *19*, 2095−2101.
(24) Mao, L.; Zhang, D.; Sotomura, T.; Nakatsu, K.; Koshiba, N.; Ohsaka, T. *Electrochim. Acta* **2003**, *48*, 1015−1021.
(25) Mao, L.; Sotomura, T.; Nakatsu, K.; Koshiba, N.; Zhang, D.; Ohsaka, T. *J. Electrochem. Soc.* **2002**, *149*, A504−A507.
(26) Gorlin, Y.; Chung, C. J.; Nordlund, D.; Clemens, B. M.; Jaramillo, T. F. *ACS Catal.* **2012**, *2*, 2687−2694.
(27) Cheng, F.; Shen, J.; Ji, W.; Tao, Z.; Chen, J. *ACS Appl. Mater. Interfaces* **2009**, *1*, 460−466.
(28) Kim, H.; Popov, B. N. *J. Electrochem. Soc.* **2003**, *150*, D56−D62.
(29) Piñero, E. R.; Khomenko, V.; Frackowiak, E.; Beguin, F. *J. Electrochem. Soc.* **2005**, *152*, A229−A235.
(30) Lee, J. S.; Lee, T.; Song, H. K.; Cho, J.; Kim, B. S. *Energy Environ. Sci.* **2011**, *4*, 4148−4154.
(31) Feng, J.; Liang, Y.; Wang, H.; Li, Y.; Zhang, B.; Zhou, J.; Wang, J.; Regier, T.; Dai, H. *Nano Res.* **2012**, *5*, 718−725.
(32) Duan, J.; Zheng, Y.; Chen, S.; Tang, Y.; Jaroniec, M.; Qiao, S. *Chem. Commun.* **2013**, *49*, 7705−7707.

(33) Lu, Y. F.; Lo, S. T.; Lin, J. C.; Zhang, W.; Lu, J. Y.; Liu, F. H.; Tseng, C. M.; Lee, Y. H.; Liang, C. T.; Li, L. J. *ACS Nano* **2013**, *7*, 6522−6532.
(34) Sheng, Z. H.; Shao, L.; Chen, J. J.; Bao, W. J.; Wang, F. B.; Xia, X. H. *ACS Nano* **2011**, *5*, 4350−4358.
(35) Zhou, X.; Wan, L. J.; Guo, Y. G. *Adv. Mater.* **2013**, *25*, 2152−2157.
(36) Liu, B.; Tian, L.; Wang, Y. *ACS Appl. Mater. Interfaces* **2013**, *5*, 8414−8422.
(37) Hwang, J. O.; Park, J. S.; Choi, D. S.; Kim, J. Y.; Lee, S. H.; Lee, K. E.; Kim, Y. H.; Song, M. H.; Yoo, S.; Kim, S. O. *ACS Nano* **2013**, *6*, 159−167.
(38) Long, D.; Li, W.; Ling, L.; Miyawaki, J.; Mochida, I.; Yoon, S. H. *Langmuir* **2010**, *26*, 16096−16102.
(39) Hummers, W. S.; Offeman, R. E. *J. Am. Chem. Soc.* **1958**, *80*, 1339−1339.
(40) Dey, R. S.; Raj, C. R. *J. Phys. Chem. C* **2010**, *114*, 21427−21433.
(41) Roy, K.; Vinod, C. P.; Gopinath, C. S. *J. Phys. Chem. C* **2013**, *117*, 4717−4726.
(42) Du, J.; Gao, Y.; Chai, L.; Zou, G.; Li, Y.; Qian, Y. *Nanotechnology* **2006**, *17*, 4923−4928.
(43) Chen, H.; Muller, M. B.; Gilmore, K. J.; Wallace, G. G.; Li, D. *Adv. Mater.* **2008**, *20*, 3557−3561.
(44) Tuinstra, F.; Koenig, J. L. *J. Chem. Phys.* **1970**, *53*, 1126−1130.
(45) Geng, D.; Yang, S.; Zhang, Y.; Yang, J.; Liu, J.; Li, R.; Sham, T. K.; Sun, X.; Ye, S.; Knights, S. *Appl. Surf. Sci.* **2011**, *257*, 9193−9198.
(46) Huang, M.; Yan, H.; Chen, C.; Song, D.; Heinz, T. F.; Hone, J. *Proc. Natl. Acad. Sci. U.S.A.* **2009**, *106*, 7304−7308.
(47) Guo, B.; Liu, Q.; Chen, E.; Zhu, H.; Fang, L.; Gong, J. R. *Nano Lett.* **2010**, *10*, 4975−4980.
(48) Buciuman, F.; Patcas, F.; Craciun, R.; Zahn, D. R. T. *Phys. Chem. Chem. Phys.* **1999**, *1*, 185−190.
(49) Paredes, J. I.; Rodil, S. V.; Alonso, A. M.; Tascón, J. M. D. *Langmuir* **2008**, *24*, 10560−10564.
(50) Gholap, S.; Badiger, M.; Gopinath, C. S. *J. Phys. Chem. B* **2005**, *109*, 13941−13947.
(51) Murugan, B.; Srinivas, D.; Gopinath, C. S.; Ramaswamy, V.; Ramaswamy, A. V. *Chem. Mater.* **2005**, *17*, 3983−3993.
(52) Joly, V. L. J.; Joy, P. A.; Date, S. K.; Gopinath, C. S. *Phys. Rev. B* **2002**, *65*, 184416/1−11.